electronics

Article

VSG Frequency Response Strategy for Doubly-Fed Wind Farm Considering the Fatigue Load

Ruichao Cui [1], Hanbo Wang [2,*], Yingming Liu [2], Xiaodong Wang [2] and Panpan Zhang [1]

[1] School of Electrical Engineering and Automation, Henan Institute of Technology, Xinxiang 453003, China; cuiruichao@hait.edu.cn (R.C.); zpp@hait.edu.cn (P.Z.)
[2] Institute of Electrical Engineering, Shenyang University of Technology, Shenyang 110870, China; lym@sut.edu.cn (Y.L.); wxd@sut.edu.cn (X.W.)
* Correspondence: wanghb@smail.sut.edu.cn; Tel.: +86-024-25670358

Abstract: A wind farm composed of doubly-fed wind turbines (DFWTs) based on the virtual synchronous generator (DFWTs-VSG) control strategy exacerbates the fatigue load on the main shaft of the DFWT-VSGs in the wind farm when responding to the frequency variation of the power system. The central controller of the wind farm can reduce the main shaft fatigue load of each DFWT-VSG by reasonably allocating the required damping coefficient of each DFWT-VSG while engaging in power system frequency response. In this study, a damping coefficient allocation method considering the main shaft fatigue load is proposed. First, a discretization equation that quantifies the relationship between the damping coefficient and its main shaft torque in DFWT-VSG is constructed. Then, based on this discretization equation, the minimization of the sum of main shaft torque fluctuation from all DFWT-VSGs is taken as the objective function in the central controller, and the constraints of the damping coefficient are set based on the support capacity of the wind farm and the operating state of each DFWT-VSG. Finally, the required damping coefficient of each DFWT-VSG is allocated in real-time based on the fmincon algorithm in the central controller. Simulation results verify the superiority of the proposed damping coefficient allocation method.

Keywords: wind farm; virtual synchronous generator; power system frequency response; main shaft fatigue load; damping coefficient allocation method

check for updates

Citation: Cui, R.; Wang, H.; Liu, Y.; Wang, X.; Zhang, P. VSG Frequency Response Strategy for Doubly-Fed Wind Farm Considering the Fatigue Load. *Electronics* **2024**, *13*, 2310. https://doi.org/10.3390/electronics13122310

Academic Editor: Ahmed Abu-Siada

Received: 24 April 2024
Revised: 4 June 2024
Accepted: 6 June 2024
Published: 13 June 2024

1. Introduction

As the proportion of wind power in the power system continues to climb, its weak support and low inertia characteristics will inevitably cause certain pressure on the system frequency stability [1]. To satisfy the frequency support requirements of the power system for wind power, a VSG control strategy is introduced into the inverter of wind turbines to slow down the rate of frequency change, increase the lowest point of frequency, and suppress the amplitude of frequency change in the power system [2–4]. However, since the wind turbine is a fatigue apparatus, focusing only on its power-frequency response characteristics during the frequency regulation process will accelerate the accumulation of fatigue load and shorten the service life [5].

M_s is also known as the low-speed shaft. M_s in the drive chain, which is installed between the rotor and the gearbox, is subjected to large and complex forces. Excessive accumulation of M_s fatigue load will continuously deteriorate the operating state of the wind turbine [6]. To minimize the M_s fatigue load, a large number of studies have been carried out at both the wind turbine and wind farm levels.

The wind turbine level: current methods to reduce the M_s fatigue load primarily involve suppressing generator torque fluctuation or increasing drive chain damping. A previous study indicated that M_{s_T} is determined by various factors such as generator torque and aerodynamic torque [7]. Based on the aforementioned analysis, the influence law of D_p on the M_s fatigue load was analyzed by adjusting D_p in the VSG to suppress doubly-fed induction generator torque fluctuation on the basis of constructing the DFWT-VSG model and combined with the M_{s_T} simulation results [8]. However, the influence of aerodynamics is neglected. Consequently, reducing the M_s fatigue load only by suppressing doubly-fed induction generator torque fluctuation when facing different wind conditions lacks theoretical support. Moreover, theoretical studies on the frequency response of DFWT-VSG considering the M_s fatigue load are currently lacking.

In terms of increasing drive chain damping, considerable research results have been achieved by designing an active damping controller to increase the damping equivalently. The active damping controller, without considering the rotor side converter control strategy, can equivalently increase the damping of the drive chain by only superimposing the generator torque reference value with the signal output from the controller [9]. Previous research investigated the effect of virtual inertia on the M_s fatigue load during the response of the wind turbine to the power system frequency and proposed an active damping controller based on the wavelet transform theory to increase the damping of the drive chain equivalently [10]. Other studies constructed an active damping controller based on the mathematical models of the wind turbine's torque-speed system and pitch-speed system [11,12]. In addition, the parameters in the designed controller were optimized using a particle swarm algorithm to further reduce the M_s fatigue load. However, the design concepts of the controllers in the above reference neglected the influence of actual operating conditions on the M_s fatigue load, which could not guarantee the effectiveness and reliability of the controller [9].

The wind farm level: different from suppressing generator torque fluctuation and increasing drive chain damping, in response to power system frequency variation, the central controller of the wind farm can reduce the M_s fatigue load of the whole wind farm by coordinating the allocation of the active power instruction value of each wind turbine considering the differences in the operating conditions among all wind turbines in the farm [13]. Additionally, the active power proportional allocation method adopted by most of the central controllers of wind farms is not conducive to the frequent frequency regulation of the wind turbines in the farm because it does not consider the influence of the M_s fatigue load [14]. Some researchers analyzed the influence of wind velocity, turbulivity, and active power instruction value of the wind turbine on M_{s_T} fluctuation and revealed the positive correlation between M_{s_T} fluctuation and the M_s fatigue load [15]. In one study, the sensitivity of M_{s_T} fluctuation to the active power instruction value at the wind turbine level was defined, and an explicit analytical equation for M_{s_T} sensitivity was derived [13]. Drawing on the existing research results [13], a recent study enhanced the sensitivity and accuracy by improving the explicit analytical equation [16]. Further investigations extended the analytic equation of the wind turbine into an analytical equation that can represent the sum of M_{s_T} fluctuations from all wind turbines in the farm and solved the active power instruction value to be received by each wind turbine in real-time in conjunction with the Quadprog algorithm [13,16]. Moreover, the minimum objective function of the sum of M_{s_T} fluctuations from all wind turbines in the farm was constructed based on the model predictive control strategy [17]. In addition, the real-time solution of the active power instruction value in the objective function was realized by using the iteration result sharing and algorithm multiplier updating mechanism in the target cascading analysis method.

However, the wind farm composed of multiple DFWT-VSGs is fundamentally different from the wind farm in the above reference in terms of the frequency regulation mechanism. In other words, each DFWT-VSG no longer relies on the active power instruction value allocated by the central controller for frequency support but utilizes the VSG control strategy to autonomously respond to the power system frequency variation characteristics for frequency support. Therefore, the research results in the above references no longer satisfy the frequency regulation needs of wind farms composed of multiple DFWT-VSGs. In addition, the current research for DFWT-VSGs focuses on the improvement of its converter control method while ignoring the effect of the M_s fatigue load. Therefore, the popularization and application of DFWT-VSGs have been somewhat constrained.

To address the above issues, a damping coefficient allocation method considering the M_s fatigue load is proposed. Firstly, the load-frequency control model of the power system containing the wind farm is constructed, and the output active power of the wind farm is subjected to per-unit processing. Subsequently, an analytical relational expression that can represent the relationship between D_p and M_{s_T} considering wind velocity and DFWT-VSG operating state is derived, which is subsequently extended into a discretization model of wind farm considering the M_s fatigue load. Then, based on this model, the minimization of M_{s_T} fluctuations from all DFWT-VSGs in the central controller of the wind farm is set as the objective function, and the constant D_p sum in the farm and DFWT-VSG operating state are set as constraints of the objective function. Finally, the central controller solves the D_p of each DFWT-VSG in real-time by using the fmincon algorithm with good convergence and allocates the derived D_p to each DFWT-VSG. Finally, the simulation results verify the superiority of the proposed allocation method of the damping coefficient.

The main contributions of this paper are as follows:

(1) A wind farm discretization model that quantifies the relationship between D_p and M_{s_T} in each DFWT-VSG is derived;
(2) The objective function for the sum of M_s fatigue loads of each DFWT-VSG is constructed, and the feasible region of D_p is determined based on the operation status of DFWT-WTGs and the EN50438 Standard;
(3) A damping coefficient allocation method considering the main shaft fatigue load is proposed to realize the reduction of the main shaft fatigue load of each DFWT-VSG in a wind farm while regulating the frequency of the power system.

The rest of this paper is organized as follows. In Section 2, a load-frequency control model of the power system containing a wind farm is constructed. In Section 3, a discretization model of wind farms is derived. In Section 4, a damping coefficient allocation method considering the main shaft fatigue load is proposed. In Section 5, the setup conditions required for simulation verification are provided, and the simulation results are analyzed and discussed in detail. Finally, this paper is concluded in Section 6.

2. Load-Frequency Control Model of a Power System with Wind Farm

To study the relationship between the sum of the output power of a doubly-fed wind farm consisting of N DFWT-VSGs, a hydroelectric farm, and a thermal farm and the power system frequency (f_{grid}), the load frequency control (LFC) model with the wind farm is constructed as shown in Figure 1. The specific parameters of the model are presented in Table 1 [18].

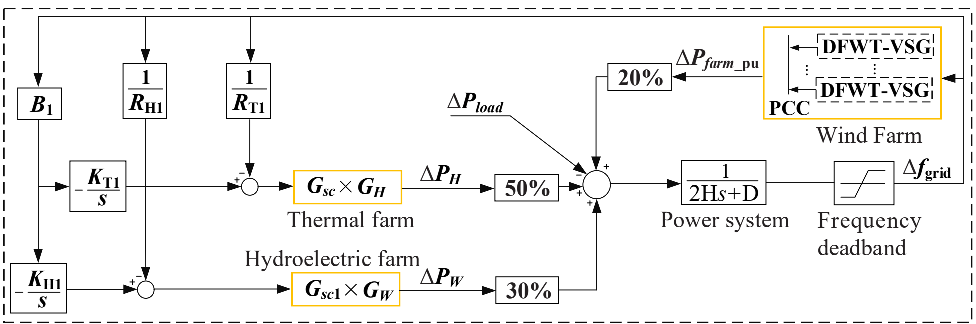

Figure 1. LFC model with wind farm.

Table 1. Parameters of LFC model.

Parameter	Value	Parameter	Value
B_1	0.425 pu	T_{TG}	0.2 s
R_{H1}	0.05 pu	T_{TR}	7.0 s
R_{T1}	0.05 pu	T_{TT}	0.3 s
K_{H1}	3 pu	R_{HP}	0.05 pu
K_{T1}	3 pu	T_{HG}	0.2 s
H	5.994 s	T_{HR}	5.0 s
D	1 pu	T_{HW}	1.0 s
R_{HT}	0.38 pu		

In Table 1, B_1 is the deviation factor, R_{H1} is the hydroelectric unit drooping coefficient, R_{T1} is the thermal unit drooping coefficient, K_{H1} is the hydroelectric unit integral controller coefficient, K_{T1} is the thermal unit integral controller coefficient, H is the equivalent inertia coefficient of the power system, D is the equivalent damping coefficient of the power system, T_{TG} is the thermal unit governor time constant, T_{TR} is the thermal unit reheat time constant, T_{TT} is the time constant of the thermal unit's main air inlet and steam box. T_{HG} is the hydroelectric unit reheat time constant, T_{HR} is the hydroelectric unit reset time, T_{HW} is the hydroelectric unit start-up time constant, R_{HT} is the hydroelectric unit short-time drooping factor, and R_{HP} is the hydroelectric unit permanent drooping factor.

ΔP_H, ΔP_W, and $\Delta P_{farm\_\mathrm{pu}}$ in Figure 1 are the active power variations output from the thermal farm, hydroelectric farm, and wind farm according to f_{grid} variation (Δf_{grid}), of which the proportions of the thermal farm, hydroelectric farm, and wind farm are 50%, 30%, and 20%, respectively. PCC is the common connection point of N DFWT-VSGs. The frequency deadband can eliminate the unfavorable effects of frequent output variations in thermal, hydroelectric, and wind farms due to the tiny Δf_{grid}.

The thermal and hydroelectric farms in Figure 1 have power reserves involved in the frequency regulation of the power system. The thermal farm consists of a governor and a reheat gas turbine. The expression for the governor is:

$$G_{sc} = \frac{1}{1 + sT_{TG}} \tag{1}$$

where s is the Laplace operator. The expression for the reheat gas turbine is:

$$G_H = \frac{1 + sT_{TR}T_{TT}}{(1 + sT_{TR})(1 + sT_{TT})} \tag{2}$$

The hydroelectric farm consists of a governor and a reheat gas turbine. The expression for the governor is:

$$G_{sc1} = \frac{1}{1 + sT_{HG}} \tag{3}$$

The expression for the hydraulic turbine is:

$$G_W = \frac{T_{HR}s + 1}{1 + sT_{HR}\frac{R_{HT}}{R_{HP}}} \frac{-T_{HW}s + 1}{1 + 0.5sT_{HW}} \tag{4}$$

The specific values of the parameters in Equations (1)–(4) are shown in Table 1 [19].

As shown in Figure 1, each DFWT-VSG in the wind farm is adjusted according to the Δf_{grid} triggered by the load change (ΔP_{load}), which generates the change in the wind farm's active power known value (ΔP_{farm}). However, since the active power of the wind farm is of the order of MW, and the LFC model adopts per-unit values for both thermal and hydroelectric farms, as shown in Table 1, ΔP_{farm} should be subjected to per-unit processing to satisfy the consistency of the power order. The expression of $\Delta P_{farm-\mathrm{pu}}$ after per-unit processing is as follows:

$$\begin{cases} \Delta P_{farm\_pu} = (\sum_{i=1}^{N} P_{total} - \sum_{i=1}^{N} P_{\mathrm{dem}}) / \sum_{i=1}^{N} P_{rated} \\ \Delta P_{farm} = \sum_{i=1}^{N} P_{total} \end{cases} \quad (5)$$

where P_{total} and P_{dem} are the sum of the known values of the stator and rotor active power output from a single DFWT-VSG and the total instruction value of the active power, respectively (MW), P_{rated} is the rated active power of the DFWT-VSG (MW), N is the total number of DFWT-VSGs in the wind farm, and i is the serial number of the DFWT-VSG.

3. Discretization Model for Wind Farm Considering M_{s_T} Fluctuation

3.1. Composition and Structure of the DFWT-VSG

To derive the analytical relational expression between D_p in the VSG control strategy and M_{s_T}, the composition and structure of the DFWT-VSG is provided in Figure 2.

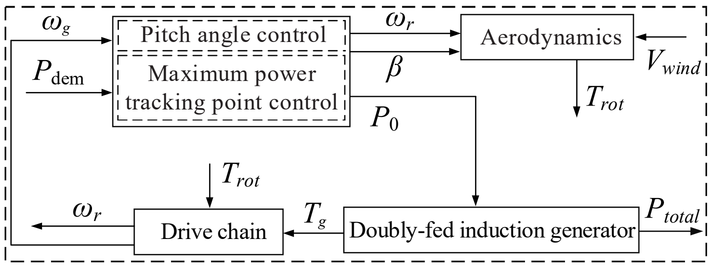

Figure 2. The Composition and Structure of DFWT-VSG.

In Figure 2, T_{rot} is aerodynamic torque (MN·m), ω_r is the angular velocity of the rotor (rad·s^{-1}), V_{wind} is the wind velocity (m/s), β is the pitch angle (rad), ω_g is rotor angular velocity of the doubly-fed induction generator (rad·s^{-1}), ω_f is the filtered rotor angular velocity (rad·s^{-1}), T_g is the torque of the doubly-fed induction generator (N·m), and P_0 is the instruction value of the stator active power (MW).

The components in Figure 2 are as follows:

① Aerodynamics

In Figure 2, the expression for T_{rot} is:

$$T_{rot} = 0.5\rho\pi R^2 C_p(\lambda, \beta) V_{wind}^3 / \omega_r \quad (6)$$

where ρ is the air density (kg/m^3), R is the blade radius (m), C_p is the wind energy power coefficient, λ is the tip speed ratio ($\lambda = \omega_r R / V_{wind}$).

② Pitch angle control

The purpose of pitch angle control in Figure 2 is to generate the pitch angle β required to adjust the blade. The expression for β is:

$$\beta = (K_{p\beta} + \frac{K_{i\beta}}{s})(\omega_f - \omega_{\mathrm{g\_rate}}) \quad (7)$$

where $K_{p\beta}$ and $K_{i\beta}$ are the proportional and integral control parameters in the pitch angle controller, respectively, and $\omega_{\mathrm{g\_rate}}$ is the rated rotor angular velocity of the doubly-fed induction generator (rad·s^{-1}). To filter out the high-frequency noise contained in ω_g, the high-frequency noise contained in ω_g needs to be processed by a low-pass filter. The rotor angular velocity (ω_f) of the filtered doubly-fed induction generator can be expressed as:

$$\omega_f = \frac{1}{1+sT_f}\omega_g \tag{8}$$

where T_f is the low-pass filter time constant (s).

③ Drive chain

As presented in Figure 2, the drive chain transmits wind power to the doubly-fed generator to generate electrical energy. The structure of the drive chain for two mass blocks is shown in Figure 3 [10]. ω_r and ω_g in Figure 3 can be expressed as follows [10]:

$$\begin{cases} J_r\frac{\mathrm{d}\omega_r}{\mathrm{d}t} = T_{rot} - K_s\theta_s - D_s(\omega_r - \omega_g/\eta_g) \\ J_g\frac{\mathrm{d}\omega_g}{\mathrm{d}t} = -T_g + \frac{D_s(\omega_r-\omega_g/\eta_g)+K_s\theta_s}{\eta_g} \\ \quad = -\frac{P_s \mathrm{n_p}}{\omega_{\mathrm{grid}}} + \frac{D_s(\omega_r-\omega_g/\eta_g)+K_s\theta_s}{\eta_g} \\ \frac{\mathrm{d}\theta_s}{\mathrm{d}t} = \omega_r - \omega_g/\eta_g \end{cases} \tag{9}$$

where J_r is the rotor inertia (kg/m^2), K_s is the stiffness coefficient of the M_s (N·m/rad), D_s is the friction damping constant of the M_s (N·m·s/rad), θ_s is the angular displacement of the main shaft (rad), η_g is the gearbox speed increasing ratio, and J_g is the inertia of the doubly-fed induction generator (kg/m^2). ω_{grid} is the angular velocity of the power system (ω_{grid} = $2\pi f_{\mathrm{grid}}$) (rad·s^{-1}). $\mathrm{n_p}$ is the pole-pair number of the doubly-fed induction generator, P_s is the known value of active power output from the stator of the doubly-fed induction generator (MW).

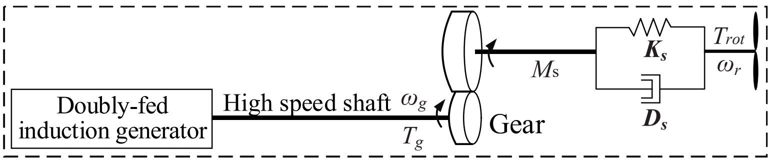

Figure 3. Drive chain.

According to reference [12], M_{s_T} can be quantified as (MN·m):

$$M_{s\_T} = K_s\theta_s + D_s(\omega_r - \omega_g/\eta_g) \tag{10}$$

Notably, the parameter values in Equations (6)–(10) are referenced to the NREL 5MW model, and their specific values are shown in Appendix C. According to reference [10], larger fluctuation in M_{s_T} leads to more M_s fatigue load accumulations. The M_s fatigue load is represented by the damage equivalent load (DEL). The DEL value is derived from the MCrunch code's calculation of the timing data for M_{s_T}.

④ MPPT control

The role of the maximum power point tracking (MPPT) control in Figure 2 is to generate the required P_0 in the VSG control strategy. According to the reference [20], the relationship between P_0 and P_{dem} is:

$$P_0 = P_{\mathrm{dem}}/(1 - s_1) \tag{11}$$

where s_1 is the slip speed (s_1 = $(\omega_{\mathrm{grid}} - \mathrm{n_p}\omega_\mathrm{g})/\omega_{\mathrm{grid}}$).

⑤ VSG control strategy

According to the synchronous generator frequency regulation principle, the active power-frequency loop in the VSG is expressed as [21]:

$$\begin{cases} \frac{P_0-P_s}{\omega_0} - D_p(\omega_{VSG} - \omega_0) = J\frac{\mathrm{d}(\omega_{VSG}-\omega_0)}{\mathrm{d}t} \\ \frac{d\theta_{VSG}}{\mathrm{d}t} = \omega_{VSG} \end{cases} \tag{12}$$

where J is the rotational inertia in the VSG (kg·m^2), D_p is the damping coefficient in the VSG (N·m·s/rad), ω_0 is the nominal angular velocity (rad·s^{-1}), ω_{VSG} is the angular velocity generated by the VSG (rad·s^{-1}), and θ_{VSG} is the angle generated by the VSG (rad).

⑥ Stator active power output from DFWT-VSG

The rotor side converter of the doubly-fed induction generator in Figure 2 enhances the DFWT's ability to support the power system frequency by utilizing a double closed-loop control strategy consisting of an outer loop comprising VSG and an inner loop comprising voltage and current [21]. According to reference [21,22], the expressions of P_s and P_{total} when DFWT-VSG is operated in parallel are:

$$\begin{cases} P_s = \frac{3u_P}{2\sqrt{R_{\mathrm{eq}}^2+X_{\mathrm{eq}}^2}}(u_s\cos\delta - u_P)\cos\varphi + \frac{3u_P}{2\sqrt{R_{\mathrm{eq}}^2+X_{\mathrm{eq}}^2}}u_s\sin\varphi\sin\delta \\ P_{total} = P_s(1-s_1) \end{cases} \tag{13}$$

where u_{p} and u_{s} are the amplitude of PCC voltage and stator voltage, respectively (V), δ is the power angle between DFWT-VSG and PCC ($\delta = \theta_{VSG} - \theta_{\mathrm{PCC}}$) (rad), and θ_{PCC} is the angle of PCC (rad). The frequency of the whole system is consistent when the power system operates in a steady state [18]. Therefore, $\omega_{\mathrm{grid}} = \omega_{\mathrm{PCC}}$ (rad·s^{-1}). ω_{PCC} is the angular frequency of PCC, and θ_{PCC} can be obtained from the integral of ω_{grid}. R_{eq} is the line resistance(Ω), X_{eq} is the line inductive reactance (Ω), and φ is the impedance angle ($\varphi = \arctan(X_{\mathrm{eq}}/R_{\mathrm{eq}})$). φ can be approximated to be 90° since X_{eq} is much larger than R_{eq} [22,23]. The following can be obtained based on Equation (13) and the above analysis [22,23]:

$$P_s \approx K\delta = K\int(\omega_{VSG} - \omega_{\mathrm{grid}})\mathrm{d}t \tag{14}$$

where $K = 1.5u_{\mathrm{p}}u_{\mathrm{s}}/X_{\mathrm{Equation}}$ According to Equations (12) and (14), the relationship between P_s and D_p can be obtained as [22]:

$$\begin{aligned} P_s &= \lim_{s\to 0}\left(\frac{K}{J\omega_0 s^2+D_p\omega_0 s+K}P_0 + \frac{K(J\omega_0 s+D_p\omega_0)}{J\omega_0 s^2+D_p\omega_0 s+K}(\omega_0 - \omega_{\mathrm{grid}})\right) \\ &= P_0 + D_p\omega_0(\omega_0 - \omega_{\mathrm{grid}}) \end{aligned} \tag{15}$$

As shown in Equation (15), in the presence of Δf_{grid}, D_p plays a decisive role in the variation of P_s. According to Equation (9), when P_s varies, ω_g and θ_s will also vary. Further, according to Equation (10), M_{s_T} varies as ω_g and θ_s vary. Based on the results of the above analysis, the research idea of coordinating and allocating D_p in each DFWT-VSG in the wind farm to reduce the sum of M_{s_T} fluctuations in the farm is feasible.

3.2. Wind Farm Discretization Model

In this study, the DEL of M_{s} (M_{s}-DEL) is reduced by suppressing M_{s_T} fluctuation in real-time. Therefore, a DFWT-VSG discretization model that can predict the state of M_{s_T} fluctuation needs to be established. Based on the coupling relationship presented between the variables in Equations (6)–(14), the continuous state-space equation of a single DFWT-VSG that can characterize the M_{s_T} fluctuation is formed as follows:

$$\begin{cases} \mathrm{d}x/\mathrm{d}t = Ax + Bu + E \\ y = Cx \end{cases} \tag{16}$$

where the state variable x is a 7 × 1 order column vector ($x = [\Delta\omega_r, \Delta\theta_s, \Delta\beta, \Delta\omega_g, \Delta\omega_f, \Delta\omega_{VSG}, \Delta P_s]^{\mathrm{T}}$), A is a 7 × 7 order state matrix, B is a 7 × 1 order column vector, E is a 7 × 1 order column vector, and C is a 1 × 7 order column vector. u is the input to Equation (16) ($u = \Delta D_p$). y is the output of the state-space equation, denoting M_{s_T} fluctuation, i.e., $y = \Delta M_{s\_T}$. The derivation processes s of A, B, C, and E are shown in Appendix A.

According to Equation (16) and Appendix A, ΔD_p has an effect on each variable in x. However, the coupling relationship between the variables in x will have an effect on ΔM_{s_T}. Therefore, ΔM_{s_T} can be changed by changing ΔD_p. Further, discretizing Equation (16) yields the relationship between $u(k)$ and $y(k+1)$ at moment k as:

$$\begin{cases} x(k+1) = A_{\mathrm{d}}x(k) + B_{\mathrm{d}}u(k) + E_{\mathrm{d}} \\ y(k+1) = Cx(k+1) \end{cases} \tag{17}$$

where $k + 1$ is the next moment of moment k. A_{d}, B_{d}, E_{d}, and C are the discretized state coefficient matrix, control coefficient matrix, constant coefficient matrix, and output state coefficient matrix, respectively, and their expressions are shown in Appendix B. The wind farm consists of N DFWT-VSGs. The wind farm discretization model can be described as follows:

$$\begin{cases} x_{total}(k+1) = A_{dtotal}(k)x_{total}(k) + B_{d\ total}(k)u_{total}(k) + E_{d\ total}(k) \\ y_{total}(k+1) = C_{total}x_{total}(k+1) \end{cases} \tag{18}$$

where $A_{\mathrm{d}total}(k)$, $B_{\mathrm{d}total}(k)$, $u_{total}(k)$, $E_{\mathrm{d}total}(k)$, $x_{total}(k+1)$, and $y_{total}(k+1)$ are the sets of the discretized matrices of each DFWT-VSG, respectively. The values of the parameters in the wind farm discretized model are shown in Appendix C. The specific expressions for $A_{\mathrm{d}total}(k)$, $B_{\mathrm{d}total}(k)$, $u_{total}(k)$, $E_{\mathrm{d}total}(k)$, $x_{total}(k+1)$, and $y_{total}(k+1)$ are shown in Appendix D.

4. Damping Coefficient Allocation Methods

4.1. Proportional Allocation Method for Damping Coefficient

The core idea of the active power proportional allocation method in the References [5,7,14,16] is to proportionally allocate the wind farm active power instruction value to each wind turbine according to the maximum active power that can be generated by each wind turbine in the farm. Without considering the M_s fatigue load, the proportional allocation method for damping coefficient (AMPDC) is adopted to realize wind farm frequency regulation referring to the idea of active power proportional allocation method. The expression of AMPDC is:

$$D_{p\ i}(k) = \frac{D_{p\ i-\max}(k)}{\sum\limits_{i=1}^{N} D_{p\ i-\max}(k)} D_{p-\mathrm{total}} \tag{19}$$

where D_{p_total} is the sum of D_p in each DFWT-VSG on the wind farm. $D_{pi}(k)$ is the D_p of the ith DFWT-VSG at the moment k. $D_{pi\_\max}(k)$ is the maximum allowable value of D_p in the ith DFWT-VSG at moment k. According to Equations (11) and (15), the following can be obtained:

$$P_{totali} = [P_{0i} + D_{pi}\omega_0(\omega_0 - \omega_{\mathrm{grid}})](1 - s_{1i}) \tag{20}$$

where P_{totali}, P_{0i}, D_{pi}, and s_{1i} are the sum of stator and rotor active power known values, stator active power instruction value, damping coefficient, and rotor slip rate output from the ith DFWT-VSG, respectively.

When $\Delta f_{\mathrm{grid}} < 0$ and crosses the frequency deadband set point, the DFWT-VSG needs to generate additional active power to reduce Δf_{grid}. In this case, the maximum output power $P_{totali\_\max}$ can be determined based on the operating state of the ith DFWT-

VSG and the capacity limitation. Moreover, $D_{pi\_\max}(k)$ can be obtained according to Equations (11), (13) and (20):

$$D_{pi\_\max}(k) = \frac{P_{totali} -_{\max}(k) - P_{\mathrm{demi}}(k)}{\omega_0(\omega_0 - \omega_{\mathrm{grid}}(k))(1 - s_{1i}(k))} \tag{21}$$

When $\Delta f_{\mathrm{grid}} > 0$ and crosses the frequency deadband set point, the DFWT-VSG needs to reduce the active power to reduce Δf_{grid}. In this case, the value of $D_{pi\_\max}(k)$ is taken based on the maximum allowable value of D_p in the standard EN50438. This standard states that when Δf_{grid} = 1 Hz, the new energy active power changes by up to 100%. Therefore, when $\Delta f_{\mathrm{grid}} > 0$, the expression for the maximum allowable value of D_p ($D_{p\_\mathrm{MAX\_EN}}$) is [24]:

$$D_{pi\_\max}(k) = D_{p\_\mathrm{MAX\_EN}} = \frac{P_{\mathrm{rated}}}{\omega_0(2\pi \times 1)} \tag{22}$$

According to Equation (22), $D_{pi\_\max}(k) = D_{p\_\mathrm{MAX\_EN}}$ when $\Delta f_{\mathrm{grid}} > 0$.

4.2. Allocation Method of Damping Coefficient Considering Main Shaft Fatigue Load

Different from the AMPDC in Section 3.1, an allocation method of damping coefficient considering main shaft fatigue load (AMDCFL) is proposed. According to the analysis of Equations (16) and (18), D_p has an effect on the operating state of each DFWT-VSG. In addition, the change in the operating state affects AMDCFL's allocation of the required D_p to each DFWT-VSG. Therefore, the AMDCFL in the central controller solves the constructed control objective based on the fmincon algorithm to reduce the sum of the M_{s} fatigue load in the farm in real-time, taking into account the coupling relationship between the operating state of each DFWT-VSG and the D_p.

4.2.1. Objective Function

Based on the wind farm discretized model constructed in Section 3.2, the expression of the objective function F is constructed as follows:

$$\min F\{D_{p1}(k), \cdots, D_{pi}(k), \cdots D_{pN}(k)\} = \left\{[y_1(k+1)]^2 + \cdots + [y_i(k+1)]^2 + \cdots + [y_N(k+1)]^2\right\} \tag{23}$$

where $y_1(k+1)$~$y_N(k+1)$ are the $\Delta M_{\mathrm{s}\_T}(k+1)$ of 1~N DFWT-VSGs at moment $k+1$, respectively. To minimize F by allocating $u_{total}(k)$ in Appendix D, Equation (18) and the equations in Appendix D need to be substituted into Equation (23). Further combining $u_i(k) = \Delta D_{pi}(k) = D_{pi}(k) - D_{pi}(k-1)$ yields the expression for F as:

$$\min F\{D_{p1}(k), \cdots, D_{pi}(k), \cdots D_{pN}(k)\} = \left\{\begin{array}{c} [a_1(D_{p\ 1}(k) - D_{p\ 1}(k-1)) + b_1]^2 \\ + \\ \vdots \\ [a_i(D_{p\ i}(k) - D_{p\ i}(k-1)) + b_i]^2 \\ + \\ \vdots \\ [a_N(D_{p\ N}(k) - D_{p\ N}(k-1)) + b_N]^2 \end{array}\right\} \tag{24}$$

where a_i and b_i can be expressed as:

$$\left\{\begin{array}{l} a_i = C_i B_{\mathrm{d}\ i}(k) \\ b_i = C_i A_{\mathrm{d}\ i}(k) x_i(k) + C_i E_{\mathrm{d}\ i}(k) \end{array}\right. \tag{25}$$

4.2.2. Constraints

As shown in Equation (24), the reasonable allocation of $D_p(k)$ of each DFWT-VSG can suppress the $M_{\mathrm{s}\_T}(k+1)$ fluctuation of 1~N DFWG-VSGs. However, if the identical relation between the sum of $D_p(k)$ and D_{p_total} of 1~N DFWT-VSGs is not taken into account, the sum of the output active power from each DFWT-VSG cannot effectively suppress Δf_{grid}, which, in turn, cannot effectively support f_{grid}. Therefore, the following equality constraint is set:

$$\sum_{i=1}^{N} D_p(k) = D_p{-}_{\text{total}} \tag{26}$$

Considering the operation state of the ith DFWT-VSG, the inequality constraint $D_{pi\_\min}(k) \leq D_{pi}(k) \leq D_{pi\_\max}(k)$ is set, where $D_{pi\_\max}(k)$ is shown in Equations (21) and (22). $D_{pi\_\min}(k)$ is the minimum allowable value of D_p of the ith DFWT-VSG at moment k. Based on Equation (15), the expression of $D_{pi\_\min}(k)$ can be obtained as:

$$\begin{cases} D_{p\ i\_\min}(k) = \frac{\zeta{-}_{\min}}{2J\omega_n} \\ \omega_{\text{n}} = \sqrt{K/(J\omega_0)} \end{cases} \tag{27}$$

where $\zeta\_{\min}$ is the minimum damping ratio of DFWT-VSG active power and ω_{n} is the natural oscillation angular frequency. According to reference [21], the damping ratio ζ exhibits a positive correlation with power stability. To ensure the operational stability of DFWT-VSG, set $\zeta\_{\min}$ = 0.7. $D_{pi\_\min}(k)$ can be derived according to Equation (27) and $\zeta\_{\min}$. $D_{pi\_\min}(k)$ in the inequality constraint ensures that ζ is within the specified range, thereby guaranteeing the stability of DFWT-VSG.

4.2.3. Solving $D_{pi}(k)$ in Real Time Based on the Fmincon Algorithm

The problem of solving $D_{pi}(k)$ for 1 to N DFWT-VSGs in Equation (24) can be regarded as a standard Quadratic Programming (QP) problem. Commercial solvers can solve this QP problem efficiently. Currently, QP problems are typically solved by population intelligence algorithms such as particle swarm optimization (PSO) and genetic algorithm (GA). However, population intelligence algorithms have several limitations, such as long computation time and unsuitability for real-time online optimization [25,26]. The Fmincon algorithm has advantages such as high solution efficiency and good convergence [27]. In version 2021a of Matlab software, the standard solution form of the fmincon algorithm is as follows:

$$M = \text{fmincon}(\text{fun},\ M\_0,\ M_{\text{A}}\ ,\ M_{\text{B}},\ M_{\text{Aeq}},\ M_{\text{Beq}},\ M_{\text{Lb}},\ M_{\text{Ub}}\ ,\ \text{nonlcon},\ \text{options}) \tag{28}$$

where M is the variable to be solved, fun is the objective function, and M_0 is the initial value of the solved variable. M_A and M_B are the linear inequality constraints of M. M_{Aeq}, and M_{Beq} are the linear equality constraints of M ($M_{Aeq} \cdot M^T = M_{Beq}$). M_{Lb} and M_{Ub} are the lower and upper limits of M, respectively. Options is the setup of options required to solve M, including iteration number, minimum error, population size, fitness, etc. nonlcon is the nonlinear constraint of M [27,28].

Comparison of Equation (23) with Equation (28) shows that M = $[D_{p1}(k), \ldots D_{pi}(k), \ldots D_{pN}(k)]$, fun = F, M_0 = $[D_{p1}(k-1), \ldots D_{pi}(k-1), \ldots D_{pN}(k-1)]$, and $D_{p1}(k-1), \ldots D_{pi}(k-1), \ldots D_{pN}(k-1)$ in Equation (28) has been solved according to the fmincon algorithm at the $k-1$ moment. Due to the absence of linear inequality constraints in the constraints set in this study, M_A = [] and M_B = [] are set in the fmincon algorithm, where [] denotes the empty set.

A comparison of Equation (26) with Equation (28) shows that M_{Aeq} consists of a matrix of 1 row and N columns, which is expressed as follows.

$$M_{\text{Aeq}} = [1,\ \cdots,1,\cdots,1] \tag{29}$$

M_{beq} = D_{p_total} in Equation (28) according to M = $[D_{p1}(k), \ldots D_{pi}(k), \ldots D_{pN}(k)]$ and Equation (29).

Comparison of Equation (21) with Equation (28) shows that M_{Ub} in Equation (28) is $D_{pi\_\max}(k)$ in Equation (21) when $\Delta f_{grid} < 0$; comparison of Equation (22) with Equation (28) shows that M_{Ub} in Equation (28) is $D_{pi\_max}(k)$ in Equation (22) when $\Delta f_{grid} > 0$. Similarly, a comparison of Equation (27) with Equation (28) shows that M_{Lb} in Equation (28) is $D_{pi\_min}(k)$.

Due to the absence of nonlinear constraints for M = $[D_{p1}(k), \ldots D_{pi}(k), \ldots D_{pN}(k)]$, nonlcon = [] is set in the fmincon algorithm. The values of the parameters in the options are shown in Table 2. $D_{pi}(k)$ is solved in real-time using the fmincon algorithm.

Table 2. The parameter values of the fmincon algorithm.

Parameter	Value
Iterations	50
Population size	50
Minimum error	1×10^{-60}
Fitness	0.03

Based on the above comparative analyses, the objective function equation, linear constraints, and upper and lower limit constraints in this study can be transformed into the corresponding solution forms of the fmincon algorithm.

Based on the above analysis, the flow of AMDCFL can be obtained, as shown in Figure 4. In Figure 4, the central controller of the wind farm invokes the fmincon algorithm to solve $D_{pi}(k)$ in real-time after constructing the objective function and solving the constraints and allocates the solved $D_{p1}(k)$~$D_{pN}(k)$ to each DFWT-VSG. Hence, the wind farm exhibits reduced ΔM_{s_T} fluctuations while responding to Δf_{grid}.

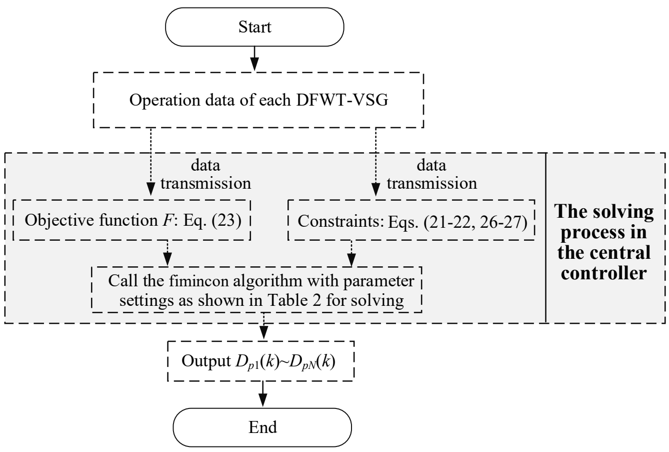

Figure 4. The flowchart of AMDCFL.

5. Case Study

5.1. Setup Conditions

A wind farm consisting of 40 DFWT-VSGs with a capacity of 5 MW was built in Matlab/Simulink, and its control structure is shown in Figure 5. When Δf_{grid} does not cross the frequency deadband, neither AMPDC nor AMDCFL in the central controller is activated. In this case, $D_p(k)$ allocated by the central controller to each DFWT-VSG can be derived according to the standard EN50438. Both reference [24] and standard EN50438 only require a $D_p(k)$ value of less than $D_{p\_MAX\_EN}$. In addition, since all DFWT-VSGs are of the same type, the value of $D_p(k)$ is set to be 700 for each of the 40 DFWT-VSGs allocated to the wind farm. In the case that Δf_{grid} crosses the frequency deadband and that either AMPDC or AMDCFL is activated, the equality constraints for both methods, i.e., D_{p_total} in Equations (19) and (26), take the value of $40 \times 700 = 28{,}000$.

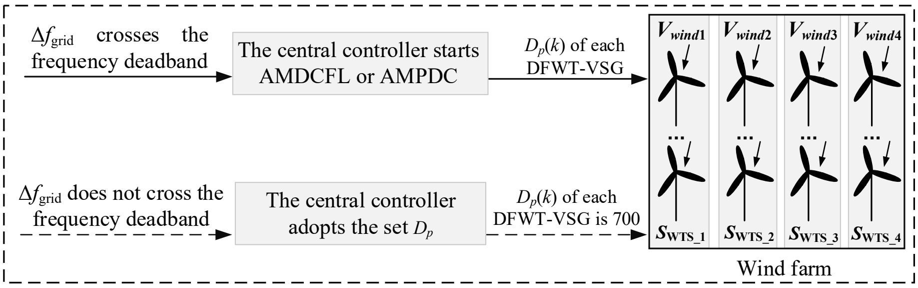

Figure 5. Control structure of wind farm.

To facilitate model construction, every 10 DFWT-VSGs in the wind farm in Figure 5 are divided into one cluster. Thus, the wind farm is divided into four clusters: $S_{\text{WTS\_1}}$, $S_{\text{WTS\_2}}$, $S_{\text{WTS\_3}}$, and $S_{\text{WTS\_4}}$. The wind velocity and the output from each DFWT-VSG in each cluster are set to be identical. In Figure 5, after collecting the state variables of each DFWT-VSG, the central controller can obtain $D_p(k)$ for 1 to N DFWT-VSGs, respectively, based on AMPDC or AMDCFL. Finally, $D_p(k)$ for 1 to N DFWT-VSGs is allocated to each DFWT-VSG to achieve the wind farm's response to Δf_{grid}.

Since the increase in average wind velocity and turbulivity exacerbates the M_{s} fatigue load [17], the V_{wind} used in each cluster is larger than the rated wind velocity, and the V_{wind} fluctuation range is between 10 m/s and 22 m/s. The range of wind velocity fluctuation for each cluster is shown in Figure 6.

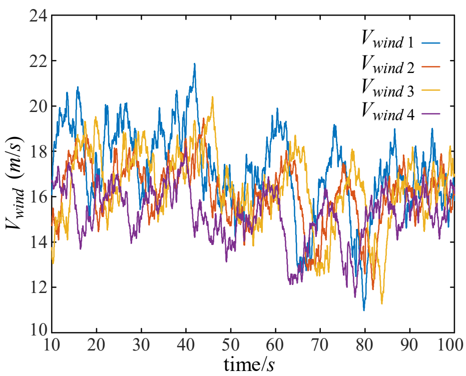

Figure 6. Wind speed of each Cluster.

To ensure enough active power allowance of the wind farm to cope with Δf_{grid}, each DFWT-VSG is reserved with 10% spare capacity. In addition, the P_{dem} of each DFWT-VSG is kept constant throughout the simulation. The total simulation duration is set to be 100 s, and ΔP_{load} occurs after 30 s. Since the wind farm completes its startup after 10 s, the time range of the simulation results is from 10 s to 100 s.

5.2. Comparative Analysis Based on the Results of AMPDC and AMDCFL

Simulation studies are carried out separately based on AMPDC and AMDCFL. Subsequently, the superiority of AMDCFL is analyzed based on the simulation results of Δf_{grid}, $\Delta P_{total\text{\_pu}}$, and M_{s} fatigue load. When ΔP_{load} occurs, the thermal farm, hydroelectric farm, and wind farm in Figure 1 jointly participate in frequency regulation. Δf_{grid} results are shown in Figure 7. As presented in Figure 7, Δf_{grid} after 30 s is continuously fluctuant. Δf_{grid} can be effectively suppressed by using AMPDC and AMDCFL, and the frequency regulation effects of AMPDC and AMDCFL are nearly the same.

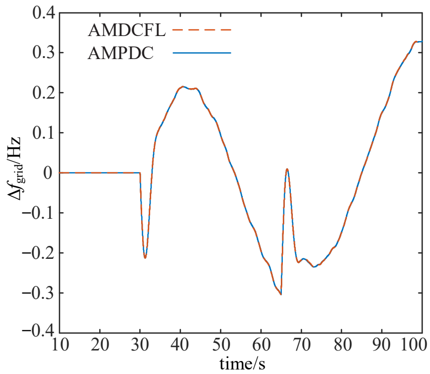

Figure 7. The results of Δf_{grid} under different allocation methods.

The results of $\Delta P_{farm\_\text{pu}}$ based on AMPDC and AMDCFL are shown in Figure 8. Influenced by the large wind velocity fluctuation, as shown in Figure 6, the $\Delta P_{farm\_\text{pu}}$ in Figure 8 has a small fluctuation between 10 s and 30 s. Since the frequency deadband set in Figure 1 can filter out Δf_{grid} caused by $\Delta P_{farm\_\text{pu}}$, $\Delta f_{\text{grid}} = 0$ in the time period of 10~30 s in Figure 7. ΔP_{load} occurs after 30 s, and Δf_{grid} breaks through the threshold set by the frequency deadband. In this case, each DFWT-VSG autonomously adjusts its own output active power based on the $D_p(k)$ output from the central controller. As shown in Figure 8, $\Delta P_{farm\_\text{pu}}$ under different allocation methods can respond to Δf_{grid} continuously and in real-time, and the $\Delta P_{farm\_\text{pu}}$ triggered by Δf_{grid} is nearly identical.

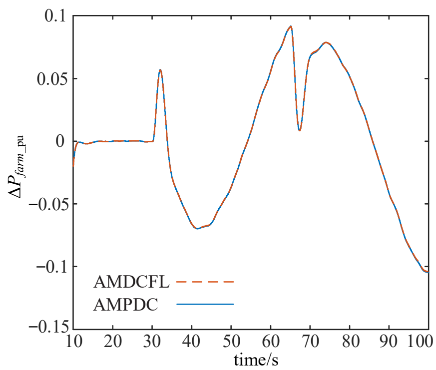

Figure 8. The results of $\Delta P_{farm\_\text{pu}}$ under different allocation methods.

In the case where the wind farm participates in frequency regulation, each cluster can reach the rated output capacity because the wind farm is in a high wind velocity scenario, as shown in Figure 6. Since M_s fatigue load is not considered in AMPDC, $D_p(k)$ obtained based on Equation (19) cannot suppress M_{s_T} fluctuation. In contrast, AMDCFL quantifies the effect of D_p on M_{s_T} according to Equations (16) and (17), taking into account the operating conditions and actual wind velocity of each DFWT-VSG. Therefore, when each DFWT-VSG responds based on the $D_p(k)$ allocated by the central controller, M_{s_T} fluctuations can be suppressed. In addition, based on the analysis of Equation (10) in the previous text, the M_{s_T} fluctuation determines the M_s fatigue load. Therefore, AMDCFL can reduce the M_s fatigue load.

To visualize the superiority of AMDCFL, the comparison results of M_{s_T} for the same DFWT-VSG among different clusters based on AMPDC and AMDCFL are provided in Figure 9.

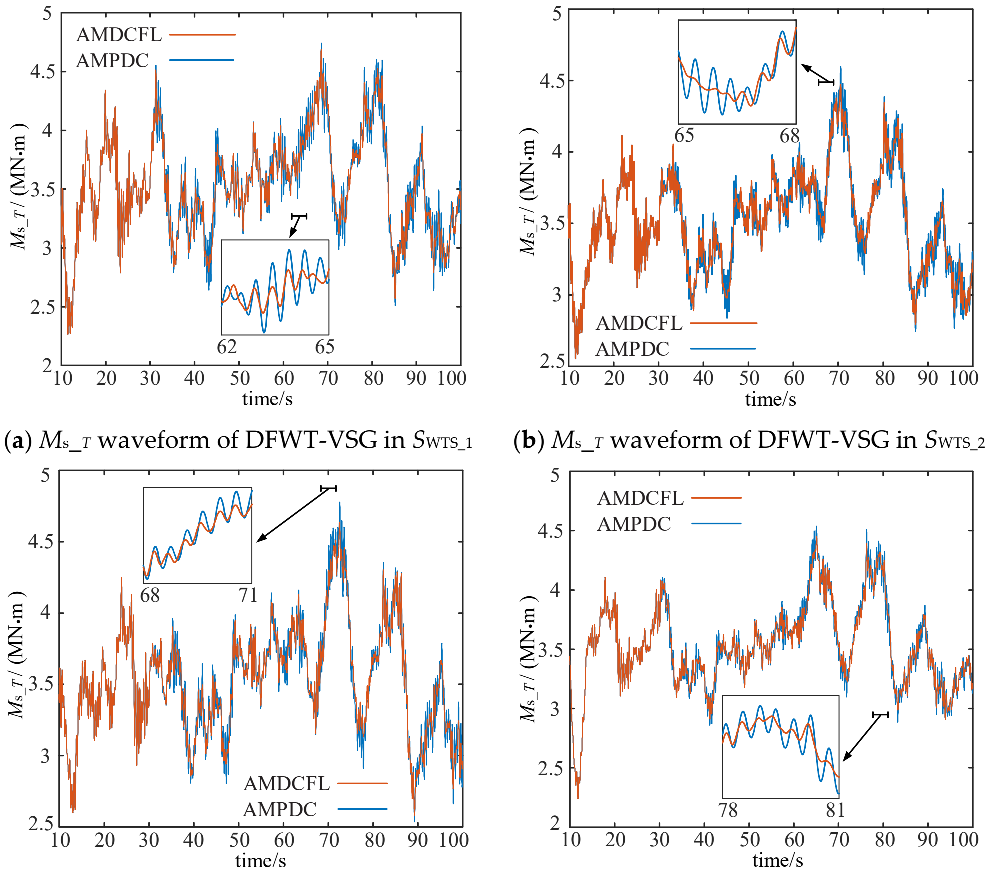

(**a**) M_{s_T} waveform of DFWT-VSG in S_{WTS_1} (**b**) M_{s_T} waveform of DFWT-VSG in S_{WTS_2}

(**c**) M_{s_T} waveform of DFWT-VSG in S_{WTS_3} (**d**) M_{s_T} waveform of DFWT-VSG in S_{WTS_4}

Figure 9. M_{s_T} waveform under different allocation methods.

According to the total fluctuations and local amplification results of M_{s_T} shown in Figure 9, compared with AMPDC, AMDCFL has significantly suppressed fluctuation amplitude of M_{s_T} taking into account wind velocity variation and operating conditions.

To visualize the superiority of AMDCFL, DEL calculations are performed on time series data forming M_{s_T} waveform based on the MCrunch code. The M_s-DEL results for each cluster at 10~100 s are shown in Table 3. As shown in Table 3, the M_s-DEL values of S_{WTS_1}, S_{WTS_2}, S_{WTS_3}, and S_{WTS_4} under AMDCFL are reduced by 6.89%, 9.49%, 8.48%, and 7.79%, respectively, compared to those under AMPDC, and the sum of M_s-DEL of each cluster within the wind farm is reduced by 8.12%.

Table 3. M_s-DEL under different allocation methods.

Cluster	**M_s-DEL/(MN·m)**	
	AMPDC	**AMDCFL**
S_{WTS_1}	32.104	29.893
S_{WTS_2}	26.393	23.889
S_{WTS_3}	31.219	28.571
S_{WTS_4}	24.384	22.485
Sum	114.100	104.838

According to Figures 7–9 and Table 3, the proposed AMDCFL can reduce the M_s-DEL of each DFWT-VSG while satisfying the frequency response, thereby prolonging the service life of DFWT-VSGs.

6. Conclusions

In the existing research results on frequency response strategies for doubly-fed wind farms considering main shaft fatigue load, none of their DFWT adopts the VSG control strategy, leading to the inapplicability of the existing research theories to doubly-fed wind farm consisting of multiple DFWTs-VSG. For this reason, this manuscript proposes AMDCFL after considering the influence of VSG control strategy on main shaft fatigue load and frequency response.

The AMPDC-based wind farm has exacerbated M_{s_T} fluctuations when responding to Δf_{grid}, thereby increasing M_s-DEL. Therefore, AMDCFL is proposed in this study to reduce M_s-DEL. This allocation method derives the analytical relational expression between D_p and M_{s_T}, considering wind velocity fluctuation and power system frequency variation. In addition, an objective function that can quantitatively represent the sum of M_s fatigue load within a wind farm is constructed. Further, based on the constraints of constant D_p sum within the wind farm, maximum active power generated by DFWT-VSG, and minimum damping ratio of DFWT-VSG, the relevant constraints of $D_{pi}(k)$ are set to guarantee frequency regulation capability of the wind farm and the operational stability of each DFWT-VSG.

The simulation results show that the adopted fmincon algorithm can effectively solve the objective function online in real-time. Compared with the AMPDC without considering the M_s fatigue load, AMDCFL not only ensures the frequency regulation capability of the wind farm but also significantly suppresses the M_{s_T} fluctuation state of each DFWT-VSG during the frequency regulation process. Compared to the sum of M_s-DEL of the AMPDC-based wind farm, the sum of M_s-DEL of the AMDCFL-based wind farm is reduced by 9.262 MN·m. The sum of M_s-DEL from all clusters in the wind farm is reduced by 8.12%. These findings demonstrate the superiority of AMDCFL.

At present, the theoretical studies for wind farms composed of DFWT-VSGs rarely consider the M_s fatigue load during frequency regulation. Therefore, the results of this study can provide certain theoretical basis and research ideas for the popularization and application of DFWT-VSG.

Moreover, the gradual increase in the number of DFWTs-VSG in future wind farm will increase the computational pressure on the AMDCFL-based central controller of wind farm, leading to the slowdown of the central controller in solving the $D_{pi}(k)$ required by each DFWT-VSG. For this reason, future research on distributed control strategies should be carried out to divert the computational pressure from the wind farm central controller.

Author Contributions: This paper was completed by the authors in cooperation. H.W. carried out theoretical research, data analysis, results analysis, and paper writing. R.C. and Y.L. provided constructive suggestions. X.W. and P.Z. revised the paper. All authors have read and agreed to the published version of the manuscript.

Funding: This work was supported by the Science and Technology Project of SGCC (Research on electromechanical coupling mechanism and control method of wind turbine during grid fault considering security constraints) (4000-202355454A-3-2-ZN).

Data Availability Statement: Derived data supporting the findings of this study are available from the corresponding author on request.

Conflicts of Interest: The authors declare no conflict of interest.

Appendix A

① $\Delta\omega_r$: $\frac{d\Delta\omega_r}{dt} = [\Delta T_{rot} - K_s\Delta\theta_s - D_s(\Delta\omega_r - \Delta\omega_g/\eta_g)]/J_r$

where ΔT_{rot} can be expressed as:

$$\Delta T_{rot} = \frac{\partial T_{rot}}{\partial\omega_r}\Delta\omega_r + \frac{\partial T_{rot}}{\partial\beta}\Delta\beta + \frac{\partial T_{rot}}{\partial V_{wind}}\Delta V_{wind}$$
$$\Downarrow$$
$$\frac{\partial T_{rot}}{\partial\omega_r} = -\frac{0.5\rho\pi R^2 V_{wind0}^3 C_{p0}}{\omega_{r0}^2} + \frac{0.5\rho\pi R^2 V_{wind0}^3}{\omega_{r0}} \cdot \frac{\partial C_p}{\partial\omega_r} \qquad \frac{\partial C_p}{\partial\omega_r} = \frac{R}{V_{wind0}} \cdot \frac{\partial C_p}{\partial\lambda}$$
$$\frac{\partial T_{rot}}{\partial\beta} = \frac{0.5\rho\pi R^2 V_{wind0}^3}{\omega_{r0}} \cdot \frac{\partial C_p}{\partial\beta} \qquad \frac{\partial C_p}{\partial\beta} \approx \frac{C_p(n,m+1) - C_{p0}}{\Delta\beta} = C_{p\_beta}$$
$$\frac{\partial T_{rot}}{\partial V_{wind}} = \frac{0.5\rho\pi R^2}{\omega_{r0}}(3V_{wind0}^2 C_{p0} - C_{p\_tsr}\omega_{r0} R V_{wind0}) \qquad \frac{\partial C_p}{\partial\lambda} \approx \frac{C_p(n,m+1) - C_{p0}}{\Delta\lambda} = C_{p\_tsr}$$

② $\Delta\theta_s$: $\frac{d\Delta\theta_s}{dt} = \Delta\omega_r - \Delta\omega_g/\eta_g$

③ $\Delta\beta$: $\frac{d\Delta\beta}{dt} = \frac{K_{p\beta}}{T_f}\Delta\omega_g + (-\frac{K_{p\beta}}{T_f} + K_{i\beta})\Delta\omega_f$

④ $\Delta\omega_g$: $\frac{d\Delta\omega_g}{dt} = [-\Delta P_s \frac{n_p}{\omega_{grid0}} + \Delta\omega_{grid}\frac{P_{s0} n_p}{\omega_{grid0}^2} + \frac{D_s(\Delta\omega_r - \Delta\omega_g/\eta_g) + K_s\Delta\theta_s}{\eta_g}]/J_g$

⑤ $\Delta\omega_f$: $\frac{d\Delta\omega_f}{dt} = -\frac{1}{T_f}\Delta\omega_f + \frac{1}{T_f}\Delta\omega_g$

⑥ $\Delta\omega_{VSG}$: $$\frac{d\Delta\omega_{VSG}}{dt} = -\frac{D_{p0}}{J}\Delta\omega_{VSG} - (\frac{\omega_{VSG0} - \omega_0}{J})\Delta D_p + \frac{1}{J\omega_0}(\Delta P_{dem}\frac{\omega_{grid0}}{n_p\omega_{g0}} - \Delta\omega_g\frac{P_{dem0}\cdot\omega_{grid0}}{n_p\omega_{g0}^2} + \Delta\omega_{grid}\frac{P_{dem0}}{n_p\omega_{g0}} - \Delta P_s)$$

⑦ ΔP_s: $\frac{d\Delta P_s}{dt} = K(\Delta\omega_{VSG} - \Delta\omega_{grid})$

According to ① to ⑦, the expressions A, B, C, and E in Equation (16) can be obtained as follows:

$$A = \begin{bmatrix} a_{11} & a_{12} & a_{13} & a_{14} & 0 & 0 & 0 \\ a_{21} & 0 & 0 & a_{24} & 0 & 0 & 0 \\ 0 & 0 & 0 & a_{34} & a_{35} & 0 & 0 \\ a_{41} & a_{42} & 0 & a_{44} & 0 & 0 & a_{47} \\ 0 & 0 & 0 & a_{54} & a_{55} & 0 & 0 \\ 0 & 0 & 0 & a_{64} & 0 & a_{66} & a_{67} \\ 0 & 0 & 0 & 0 & 0 & a_{76} & 0 \end{bmatrix} B = [0\ 0\ 0\ 0\ 0\ b_{61}\ 0]^T$$
$$C = [c_{11}\ c_{12}\ 0\ c_{14}\ 0\ 0\ 0]\ E = [e_{11}\ 0\ 0\ e_{14}\ 0\ 0\ e_{17}]^T$$

Note: Except for ω_0, the subscript 0 indicates the initial value corresponding to the parameter.

Appendix B

$$A_d = e^{AT_s} B_d = \int_0^{T_s} e^{AT_s} B dt E_d = \int_0^{T_s} e^{AT_s} E dt$$

Note: T_s is the control cycle.

Appendix C

Table A1. Parameter values of wind farm discretization equation.

Parameter	Value	Parameter	Value
R_{eq}	0.000105 Ω	X_{eq}	0.0038 Ω
J	10 kg·m^2	D_{p_total}	28,000 N·m·s/rad
$K_{p\beta}$	−0.2143	$K_{i\beta}$	−20.0918
ω_0	100 π rad·s^{-1}	ω_{g_rate}	122.9 rad·s^{-1}
u_s	$690\sqrt{2}/\sqrt{3}$ V	u_p	$690\sqrt{2}/\sqrt{3}$ V
J_r	3.54×10^7 kg·m^2	η_g	97
J_g	534.116 kg·m^2	n_p	3
D_s	6,215,000	K_s	867,637,000
T_f	0.9806		

Appendix D

$$\begin{cases} x_{total}(k+1) = [x_1(k+1), x_2(k+1)\ldots, x_N(k+1)]^{\mathrm{T}} \\ x_{\ total}(k) = [x_1(k), x_2(k)\ldots, x_N(k)]^{\mathrm{T}} \\ u_{total}(k) = [u_1(k), u_2(k)\ldots, u_N(k)]^{\mathrm{T}} \\ y_{\ total}(k+1) = [y_1(k+1), y_2(k+1), \ldots, y_N(k+1)]^{\mathrm{T}} \\ A_{\mathrm{d}\ total}(k) = diag[A_{\mathrm{d}1}(k), A_{\mathrm{d}2}(k), \ldots A_{\mathrm{d}N}(k)]^{\mathrm{T}} \\ B_{\mathrm{d}\ total}(k) = diag[B_{\mathrm{d}1}(k), B_{\mathrm{d}2}(k), \ldots B_{\mathrm{d}N}(k)]^{\mathrm{T}} \\ C_{total} = diag[C_1, C_2, \ldots C_N]^{\mathrm{T}} \\ E_{\mathrm{d}\ total}(k) = [E_{\mathrm{d}1}(k), E_{\mathrm{d}2}(k), \ldots E_{\mathrm{d}N}(k)]^{\mathrm{T}} \end{cases}$$

References

1. Shi, T.; Xu, Z.; Gu, L.; Zhou, H. Research on Fast Frequency Response Control Strategy of Hydrogen Production Systems. *Electronics* **2024**, *13*, 956. [CrossRef]
2. Zou, P.; Meng, J.; Wang, Y. Influence Analysis of the Main Control Parameters in FVSG on the Frequency Stability of the System. *High Volt. Eng.* **2018**, *44*, 1335–1342.
3. Abuagreb, M.; Allehyani, M.F.; Johnson, B.K. Overview of virtual synchronous generators: Existing projects, challenges, and future trends. *Electronics* **2022**, *11*, 2843. [CrossRef]
4. Babu, V.V.; Roselyn, J.P.; Nithya, C.; Sundaravadivel, P. Development of Grid-Forming and Grid-Following Inverter Control in Microgrid Network Ensuring Grid Stability and Frequency Response. *Electronics* **2024**, *13*, 1958. [CrossRef]
5. Yang, W.; Wen, Y.; Zhang, W.; Deng, B. Bi-level Frequency Response Control Strategy Based on Wind Power and Energy Storage. *Autom. Electr. Power Syst.* **2022**, *46*, 184–193.
6. Wang, Y.; Guo, Y.; Chen, Y.; Xu, W. Analysis of Frequency Regulation Capability and Fatigue Loads of Wind Turbine Based on Over-Speed Control. *Electronics* **2023**, *12*, 2009. [CrossRef]
7. Liu, Y.; Wang, Y.; Wang, X.; Miao, Y. Optimal Active Power Dispatch for Wind Farm Based on the Improved Fatigue Load Sensitivity. *J. Renew. Sustain. Energy* **2019**, *11*, 033306. [CrossRef]
8. Jiang, D.; Mo, R.; Yang, C.; Jia, Y.; Hu, Y.; Li, H. Dynamic Characteristics Analysis of Drive Train of Doubly-fed Wind Turbines Under Virtual Synchronous Control. *Acta Energiae Solaris Sin.* **2023**, *44*, 412–419.
9. Liu, H.; Tang, Q.; Su, Y.; Wei, L. A survey on electrical control methods of large wind turbine active vibration reduction. *J. Electr. Power Sci. Technol.* **2016**, *31*, 182–194.
10. Wang, Y.; Guo, Y.; Zhang, D.; Liu, H.; Song, R. Analysis and mitigation of the drive train fatigue load for wind turbine with inertial control. *Int. J. Electr. Power Energy Syst.* **2022**, *136*, 107698. [CrossRef]
11. Liu, Y.; Zhang, S.; Wang, X.; Gao, X.; Cao, T. Optimization of Torque Control Parameters for Wind Turbine Based on Drive Chain Active Damping Control. *IEEE Access* **2022**, *10*, 106482–106494. [CrossRef]
12. Liu, Y.; Zhang, S.; Wang, X.; Xie, H.; Cao, T. Optimization of Pitch Control Parameters for a Wind Turbine Based on Tower Active Damping Control. *Energies* **2022**, *15*, 8686. [CrossRef]
13. Zhao, H.; Wu, Q.; Huang, S.; Shahidehpour, M.; Guo, Q.; Sun, H. Fatigue Load Sensitivity-Based Optimal Active Power Dispatch for Wind Farms. *IEEE Trans. Sustain. Energy* **2017**, *8*, 1247–1259. [CrossRef]
14. Qi, Y.; Yang, H.; Yu, L. Distributed Automatic Generation Control of Wind Farm Considering Load Suppression. *Trans. China Electrotech. Soc.* **2022**, *37*, 10.

15. Huang, S.; Wu, Q.; Guo, Y.; Rong, F. Hierarchical Active Power Control of DFIG-Based Wind Farm with Distributed Energy Storage Systems Based on ADMM. *IEEE Trans. Sustain. Energy* **2020**, *11*, 1528–1538. [CrossRef]
16. Liu, Y.; Wang, Y.; Wang, X.; Zhu, J.; Lio, W.H. Active power dispatch for supporting grid frequency regulation in wind farms considering fatigue load. *Energies* **2019**, *12*, 1508. [CrossRef]
17. Yang, W.; Wen, Y.; Li, L.; Wang, K.; Chi, F.; Zhang, W. Decentralized frequency response strategy for wind farm considering fatigue load. *Electr. Power Autom. Equip.* **2022**, *42*, 55–62.
18. Wang, H.; Liu, Y.; Wang, X.; Guo, G.; Wang, L. Dynamic synthetic inertial control method of wind turbines considering fatigue load. *Front. Energy Res.* **2023**, *10*, 1067896. [CrossRef]
19. Wang, X.; Wang, Y.; Liu, Y. Dynamic load frequency control for high-penetration wind power considering wind turbine fatigue load. *Int. J. Electr. Power Energy Syst.* **2020**, *117*, 105696.1–105696.11. [CrossRef]
20. Ling, Y. Modeling, simulation, and control of doubly fed wind power generation systems. *China Mach. Press* **2018**, *6*, 209.
21. Liu, Y.; Wang, H.; Wang, X.; Guo, G.; Jing, H. Control Strategy and Corresponding Parameter Analysis of a Virtual Synchronous Generator Considering Frequency Stability of Wind Power Grid-Connected System. *Electronics* **2022**, *11*, 2806. [CrossRef]
22. Xie, Z.; Meng, H.; Zhang, X.; Jin, X.W. Virtual Synchronous control Strategy of DFIG-based Wind Turbines Based on Stator Virtual Impedance. *Autom. Electr. Power Syst.* **2018**, *42*, 8.
23. Jun, Q.; Yuanchao, L.; Hui, T.; Dan, Z.; Youbing, Z. Second-order Power De-coupling Control in Pre-synchronized VSG Based on Dynamic Virtual Current Feedforward Control. *Power Syst. Technol.* **2020**, *44*, 9.
24. Sheng, W.; Lv, Z.; Cui, J. Operation Area Calculation and Parameter Analysis of Virtual Synchronous Generator. *Power Syst. Technol.* **2019**, *43*, 1557–1565.
25. Júnior, G.A.N.; Martins, M.A.; Kalid, R. A PSO-based optimal tuning strategy for constrained multivariable predictive controllers with model uncertainty. *ISA Trans.* **2014**, *53*, 560–567. [CrossRef]
26. Gong, D.; Fang, J. Optimizing interval higher-dimensional multi-objective problems using a set-based evolutionary algorithm incorporated with preferences. *Control Theory Appl.* **2013**, *30*, 1369–1383.
27. Sreeraj, P. Prediction and optimization of weld bead geometry in gas metal arc welding process using RSM and fmincon. *J. Mech. Eng. Res.* **2013**, *5*, 154–165. [CrossRef]
28. Chen, Z.; Li, Z.; Chen, G. Optimal configuration and operation for user-side energy storage considering lithium-ion battery degradation. *Int. J. Electr. Power Energy Syst.* **2023**, *145*, 108621. [CrossRef]